

Tracking granules at the Sun's surface and reconstructing velocity fields. II. Error analysis

R. Tkaczuk¹, M. Rieutord¹, N. Meunier², T. Roudier²

¹ Laboratoire d'Astrophysique de Toulouse et Tarbes, UMR 5572, CNRS et Université Paul Sabatier Toulouse 3, 14 avenue E. Belin, 31400 Toulouse, France

² Laboratoire d'Astrophysique de Toulouse et Tarbes, UMR 5572, CNRS et Université Paul Sabatier Toulouse 3, 57 Avenue d'Azereix, BP 826, 65008 Tarbes Cedex, France

e-mail: tkaczuk@ast.obs-mip.fr, rieutord@ast.obs-mip.fr, meunier@ast.obs-mip.fr, roudier@ast.obs-mip.fr

Received ; Accepted

ABSTRACT

Context. The determination of horizontal velocity fields at the solar surface is crucial to understanding the dynamics and magnetism of the convection zone of the sun. These measurements can be done by tracking granules.

Aims. Tracking granules from ground-based observations, however, suffers from the Earth's atmospheric turbulence, which induces image distortion. The focus of this paper is to evaluate the influence of this noise on the maps of velocity fields.

Methods. We use the coherent structure tracking algorithm developed recently and apply it to two independent series of images that contain the same solar signal.

Results. We first show that a $k - \omega$ filtering of the times series of images is highly recommended as a pre-processing to decrease the noise, while, in contrast, using destretching should be avoided. We also demonstrate that the lifetime of granules has a strong influence on the error bars of velocities and that a threshold on the lifetime should be imposed to minimize errors. Finally, although solar flow patterns are easily recognizable and image quality is very good, it turns out that a time sampling of two images every 21 s is not frequent enough, since image distortion still pollutes velocity fields at a 30% level on the 2500 km scale, i.e. the scale on which granules start to behave like passive scalars.

Conclusions. The coherent structure tracking algorithm is a useful tool for noise control on the measurement of surface horizontal solar velocity fields when at least two independent series are available.

Key words. Convection – Turbulence – Sun: granulation – Sun: photosphere

1. Introduction

Movies of the solar surface show that it is a place of intense turbulent fluid flows where three major scales (granulation, mesogranulation, and supergranulation) have been pointed out. In order to better understand the underlying dynamics, it is crucial to be able to measure the velocity fields. As far as horizontal flows are concerned, the basic techniques have relied on measuring the displacement of granules that, as shown by Rieutord et al. (2001), trace the fluid flows on scales larger than 2.5 Mm.

Two algorithms have been devised to transform a time sequence of images into a sequence of horizontal velocity fields maps. These are the LCT algorithm (i.e. local correlation tracking, see November & Simon 1988) and the CST algorithm (coherent structure tracking, see Rieutord et al. 2007 hereafter referred to as Paper I).

When the surface velocity field is known, one is usually interested in identifying/following the dynamical structures of the flow - like vortices, upwellings, or downwellings. The identification of these structures demands, however, computing the velocity gradients like the divergence or the vorticity. In Paper I, it has been pointed out that such quantities are very sensitive to the noise induced by terrestrial atmospheric distortion, since they are derivatives of the velocity field. The use of the velocity field to describe the dynamics of the solar surface thus needs to be complemented by an error analysis that both evaluates the significance of the observed dynamical features and gives a way to eliminate, or at least reduce, the impact of errors.

The aim of this paper is to analyse the consequences of errors in the final result of velocity, vorticity, and divergence fields. As mentioned above, the main source of errors comes from the distortion of images induced by the Earth's atmospheric turbulence. The case

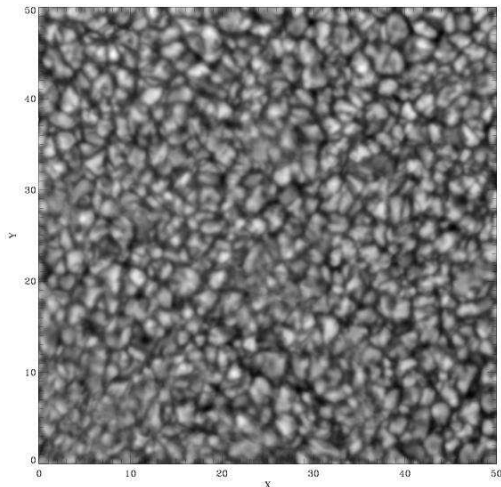


Fig. 1. View of the region used for the tests. X and Y scales are in arcsec.

of errors or, equivalently, the precision of measurements has already been discussed for the LCT algorithm by November & Simon (1988), who mentioned errors the order of 20 m/s on the velocity field. Further work by Simon et al. (1995) showed that this precision was certainly largely overestimated. More recently, Potts et al. (2003) investigated the case of interpolation errors, associated with the LCT algorithm, which also spoil the final result. Here, we focus on the CST algorithm and try to give a neat picture of the influence of the Earth's atmospheric distortion on the measurement of the velocity fields on different scales.

We organised the paper as follows. Using two independent series of images of the solar surface, we first evaluate the noise induced on the positions of the granules and how image pre-processing can reduce it. We then focus on the way the noise influences the final velocity fields on different scales and analyse its propagation up to the curl and divergence maps. Conclusions and outlooks follow.

2. Observations

We use a time series of images obtained on June 5, 1993 at the SVST (Swedish Vacuum Solar Telescope), Observatorio Roque de los Muchachos, La Palma (data courtesy of P. Brandt, see also Simon et al. 1994). This data set has already been studied by many authors (Sobotka et al. 1997a,b; Sobotka et al. 1999a,b; Dorotovič et al. 2002; Getling & Brandt 2002; Roudier et al. 2003). The original series consists of 1868 image pairs of size 1310×970 pixels taken at $\lambda = 468 \pm 5$ nm. The time between two pairs of images is close to 21 seconds. Images from a pair are separated by a few seconds (3 s on average and always less than 14 s). The pixel size is $0''.125$, and the spatial resolution is near the diffraction limit $0''.25$. The field of view is $2'.7 \times 2'.0$. However, the instrument leads to a rotation of the field of view, and the area observed on the Sun at the beginning of the time

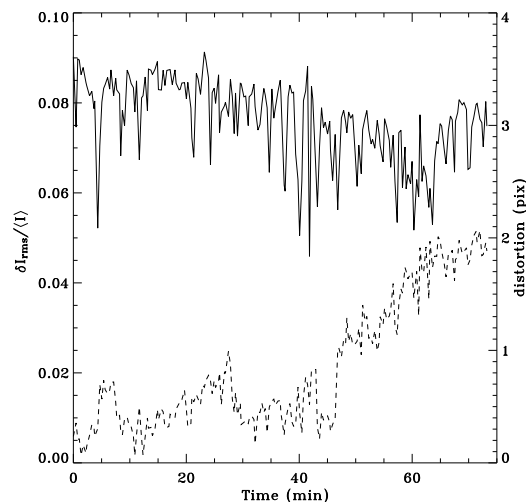


Fig. 2. Indices of image quality. Contrast (solid line) and distortion amplitude (dashed line, scale on right). Distortion is the rms displacement, evaluated with local correlation tracking, between two images of a pair.

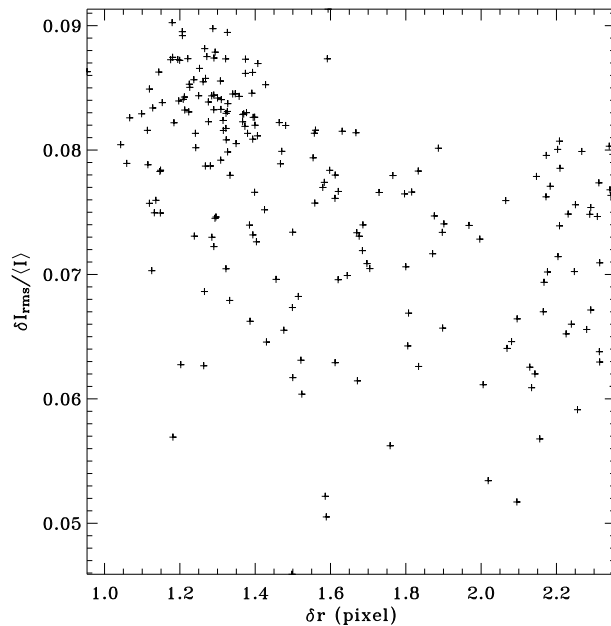


Fig. 3. The normalized intensity contrast versus the rms displacement of granules between the two images of each pair.

series is different from the one at the end. The rotation centre is located on a pore at pixel coordinates (590, 102) (not in the field-of-view used here).

For our investigations described below, we used a sub-sample of 210 pairs of frames (images 841 to 1262), covering ~ 77 minutes. In Sect. 6, slightly more data have been used (images 800 to 1298 corresponding to a ~ 87 min sequence). As shown in Fig. 1, we extract a region of 401×401 pixels centred on a (magnetically) quiet zone.

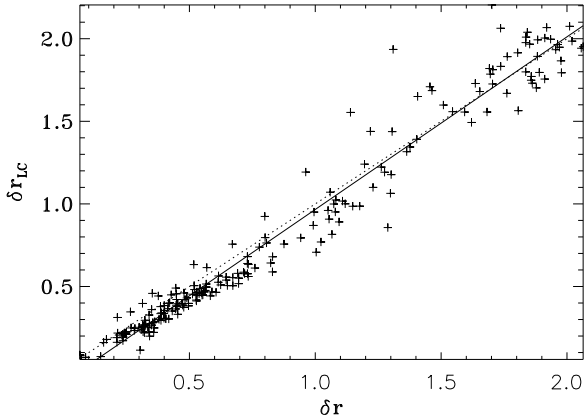


Fig. 4. Mean distance between granule centres of gravity for each image pair versus the mean displacement due to atmospheric turbulence estimated by local correlation (one point per image pair). Both displacements are in pixels. The solid line shows the line of equation $y = x$ and the dotted line is a linear fit over the points.

The main advantage of this data set is that it contains two independent sequences of images that can be considered as representing the same solar signal. The only difference comes from the Earth’s atmospheric distortion, the effects of which can thus be analysed. Moreover, as shown by Fig. 2, image quality varies during the sequence. Although the contrast remains almost constant, we see that the amplitude of distortion increases after $t=45$ min. We thus have at our disposal a “good” sequence where mean distortion is about 0.5 pixel and a “bad” sequence, where mean distortion reaches an amplitude of 2 pixels. In the following when we refer to “good” data, we mean the first 45 min, while “bad” data will designate the remaining sequence.

3. Sources of errors in CST

In the CST method, errors are introduced through the segmentation (i.e. through determination of the granule positions) and through interpolation done in order to obtain a velocity field sampled over a regularly-spaced grid. The precision at which the velocity field can be measured thus depends on:

- the precision at which a granule position is determined,
- the duration of granule tracking,
- the temporal resolution (time interval between velocity maps),
- the spatial resolution of the grid used to sample the velocity field.

This list shows that the CST algorithm allows us to identify all the crucial steps and thus to follow the propagation of errors from the beginning to the end of the computation.

4. Standard deviation of granule positions

The first step in the error analysis is to estimate the error on the granule positions¹. We first apply it to the raw data, and then use it to estimate the performances of pre-processing steps that can be performed before granule segmentation, namely on the image sequences.

4.1. Method

To estimate the standard deviation on granule positions, we use pairs of images. Because of their quasi-simultaneity, they represent the same solar surface, and all the differences between them come from atmospheric distortions, instrumental effects, or processes applied on the data.

After the segmentation step, the algorithm identifies granules present in both images of the pair. We then simply measure the distance between two identical granules. More precisely, we consider that the position of a granule is controlled by two random variables (x_i, y_i) for which we have two realisations. We thus construct two other random variables $(\delta x_i, \delta y_i) = (x_{i,1} - x_{i,2}, y_{i,1} - y_{i,2})$, whose variance is just twice that of (x_i, y_i) . Thus with a pair of images we can estimate the mean error over the field of view in each direction x and y by

$$\sigma_x = \sqrt{\frac{1}{2N} \sum_{i=1}^N (x_{i,1} - x_{i,2})^2}, \quad \sigma_y = \sqrt{\frac{1}{2N} \sum_{i=1}^N (y_{i,1} - y_{i,2})^2},$$

and the mean displacement $\delta r = \sqrt{\sigma_x^2 + \sigma_y^2}$.

These quantities are clearly estimates of the image quality through atmospheric distortion. Interestingly enough, we compared this estimate with the intensity contrast usually used to indicate image quality. As shown in Fig. 3, the correlation between the two indicators is rather poor, meaning that they are largely decoupled although they both come from atmospheric turbulence! We interpret this result, tentatively, as showing that different layers of the Earth’s atmosphere control the contrast and the distortion.

Furthermore, we compared (see Fig. 4) the displacement of granules with the displacement field derived from a local correlation tracking (using an FWHM of 20 pixels) between the two images of a pair. As expected, the correlation is much better (~ 0.96).

4.2. Application to pre-processing

One of the interesting applications of the error estimate on the granule position is to allow the evaluation of the effectiveness of various pre-processings applied to the images before estimating the granule position. A measure of σ_x before and after a given pre-processing indicates its performance. We have applied this approach to the $k - \omega$ filtering and to the destretching.

¹ By granule position we mean the position of the centre of gravity of the granule in the segmented image.

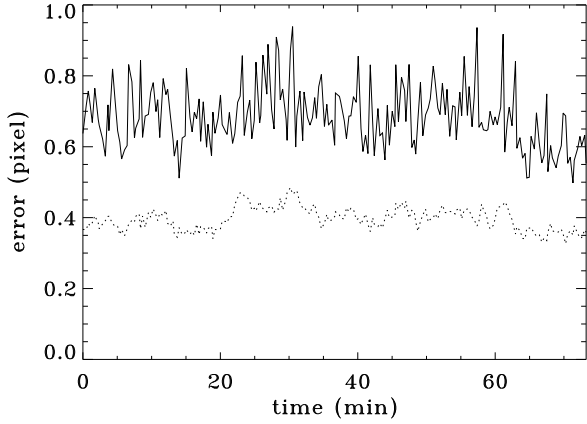


Fig. 5. Estimation of the error σ_x on the determination of the centre of gravity position in the x direction as a function of time with no $k - \omega$ filtering (solid line) and with the filtering (dotted line).

Good data			
	σ_x	σ_y	N_g
No processing	0.696 ± 0.081	0.701 ± 0.084	1077 ± 91
$k - \omega$	0.416 ± 0.037	0.418 ± 0.028	1096 ± 34
Bad data			
	σ_x	σ_y	N_g
No processing	0.694 ± 0.075	0.727 ± 0.079	803 ± 150
$k - \omega$	0.470 ± 0.039	0.527 ± 0.045	972 ± 89

Table 1. Comparison of the performances obtained on time series with high and low quality images with and without $k - \omega$ filtering.

4.2.1. $k - \omega$ filtering

The $k - \omega$ filtering (see for example Title et al., 1987) acts both spatially and temporally. In practice, it is a thresholding in the Fourier space. The contributions of all frequencies corresponding to a phase velocity higher than the threshold are eliminated.

Let us note that the data we use are irregularly sampled. The time step between two pairs of images is about 21 seconds, within a few seconds (the maximum deviation with respect to a periodic sampling is 15 s, while the average deviation is 6.3 s). The same data set has been used by Dorotovič et al. (2002), who interpolated them to get a regularly spaced time series. We consider that this is an unnecessary refinement since, within a few seconds, the solar signal does not change. Hence, with a regular time step, images would differ from ours by just a different realisation of the Earth’s atmospheric turbulence.

Figure 5 shows the average pixel error on the x -position of the granules for data pre-processed with a $k - \omega$ filtering and data without pre-processing. We used a threshold for the phase velocity of 4 km/s. The figure shows that the performance is quite improved over the whole time series by the use of this filtering. The error for the y -component

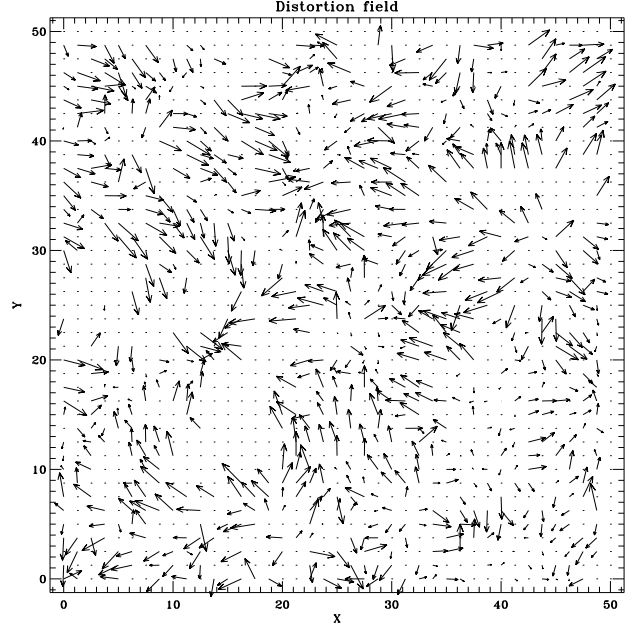


Fig. 6. An example of a map of displacements due to the Earth’s atmospheric distortion as sampled by granules. Regions without data have too low an image quality for a granule to be identified. X and Y are in arcsec.

is within an order of magnitude of the error for the x -component.

One may wonder why the increasing distortion seen after $t=45$ min in Fig. 2 does not appear in Fig. 5. This comes from the way the error is measured. Indeed, only granules close enough in a given pair of images are kept. The distortion map in Fig. 6 shows the lack of measurements in some regions: image quality is not good enough for granules to be identified from one frame to the other. With this method it is clear that high-amplitude distortion does not show up with increased error in granule position, but instead appears in a reduction of the number of “valid granules”. In Fig. 7 we see the loss of granules when conditions deteriorate and how $k - \omega$ filtering improves the situation. Numbers in Table 1 also illustrate this process. The errors only slightly increase from the “good” to the “bad” data, but the number of granules, and in other words the number of measuring points, is reduced by 20% without filtering, while the loss is 10% with filtering.

4.2.2. Destretching

This method, introduced by November & Simon (1988), is based on the same principles as the LCT. It uses a local correlation scheme to determine the displacements with respect to a reference image. From these displacements, images are stretched by interpolation in order to be the closest possible to the reference image. This method aims at correcting the effects of atmospheric turbulence and

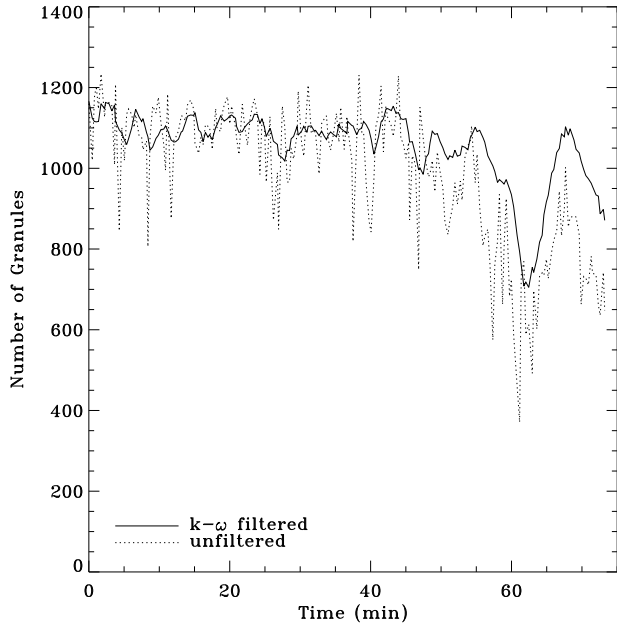


Fig. 7. Comparison of the number of granules for each image for raw data (dotted line) and for $k - \omega$ filtered data (solid line). The number of granules is defined as the number common to both images taken ‘simultaneously’. We note that filtering attenuates the fluctuations and when atmospheric distortion increases, filtering reduces the losses of granules.

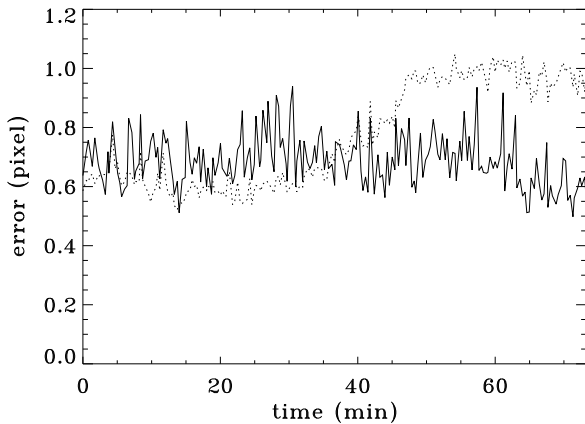


Fig. 8. Same as Fig. 5 but for destretching; the solid line is for unprocessed data, while dotted lines show the error (σ_x) with the destretched sequence.

allows us to compare images that are then plagued with the same distortion.

The pre-processing we used applies 4 successive corrections based on local correlation tracking with the following parameters: an FWHM of 31 pixels with a 62 pixel step, an FWHM of 62 pixels and a 31-pixel step, a 32 FWHM and a 16-pixel step, and then an FWHM of 20 pixels and a 10-pixel step. This combination has been established em-

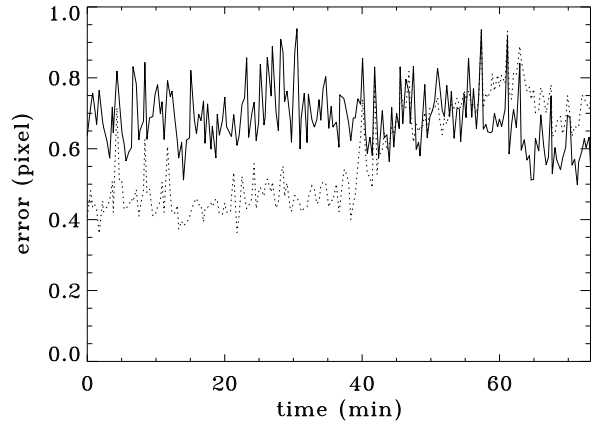


Fig. 9. Efficiency of destretching: the dotted line shows the difference between two simultaneous images when one has been destretched with the other as reference.

pirically and seems to give the best results. We remind that 62 pixels correspond to $7.75''$ and 10 pixels to $1.25''$.

Figure 8 compares the error estimate on the granule positions in the x -direction between the destretched and raw time series. Note that when image quality is good ($t \leq 45$ min) errors remain of the same order of magnitude as in raw data but fluctuations are less important, while when image quality decreases ($t > 45$ min), errors increase. Quite clearly the destretched series does not compare favourably with the raw one. On the contrary, destretching seems to worsen the results when the image quality is slightly degraded.

Actually, the poor performance of destretching on error reduction could be anticipated from the result displayed in Fig. 9. There we plot the mean distance between the granules in two simultaneous plates when one plate has been destretched to the other. If destretching were perfect, the error would vanish. Clearly, this is not the case: in the sequence with ‘intense’ atmospheric turbulence the error is not reduced at all, while during the good sequence, a small factor 1.5 is gained. Therefore we interpret the error increase generated by destretching as evidence that the destretching process decorrelates from the true displacement of granules and thus introduces a new random variable whose dispersion adds to the original signal as shown by the factor $\sqrt{2}$ taken by the error. This decorrelation may probably come from a change in scale of the distortion motions that is no longer matched by the destretching process optimized for the first frames of the sequence. If this interpretation is correct, the destretching process would need a readjustment of the local correlation tracking parameters from time to time, making the whole processing very costly computationally. The only good point introduced by destretching is the reduction of the fluctuations.

Resolution	σ_x	$\sigma_x(k-\omega)$
1''25	0.72	0.42
2''50	0.37	0.18
5''00	0.28	0.11
10''0	0.20	0.08

Table 2. Rms fluctuations of the position of granules on a typical pair of images shown for different resolutions with the multi-resolution analysis and with and without $k-\omega$ filtering. σ_x are given in image pixel. The 1''25 resolution corresponds to unfiltered data.

4.2.3. Distortion noise on different scales

We have shown in Paper I that multi-resolution analysis was an interesting tool for the determination of flow structures. We may thus wonder how the distortion noise affects the different scales and therefore resists to wavelet filtering. Using maps such as the one in Fig. 6 we compute the different components of a multi-resolution decomposition as will be used in the analysis of the velocity field. Quantitatively we show in Table 2 the values of the distortion amplitude on different scales. This table again shows the importance of $k-\omega$ filtering in the reduction of errors, especially on large scales.

4.2.4. Conclusion

To conclude this section, two points should be underlined. On the one hand, destretching is certainly an unnecessary complication whose only positive effect is to reduce the noise fluctuations when correctly tuned to the distortion scales; otherwise, it is likely to double the variance of the signal. On the other hand, $k-\omega$ filtering appears as the required pre-processing whose effect on noise reduction is clear. We surmise that, when using time-sequences with a higher time-sampling, the noise reduction by $k-\omega$ filtering will be even more efficient.

5. Propagation of errors from granule positions to the velocities

After examining the estimation of errors on the granule position in the previous section, we now study the propagation of these errors to the velocity of the granules, after averaging in time and over a given spatial range.

5.1. Error propagation

As seen above, the first step of the velocity computation in the CST algorithm is to determine of the position of granules on each image. The duration of the tracking of the k^{th} granule is given by $\Delta t_k = t_{n_f(k)} - t_{n_i(k)}$, where $n_i(k)$ is the image where the granule k appears and $n_f(k)$ the image where it disappears.

Over an image, granules are much less dense than pixels, making the velocity field sampled on a much coarser

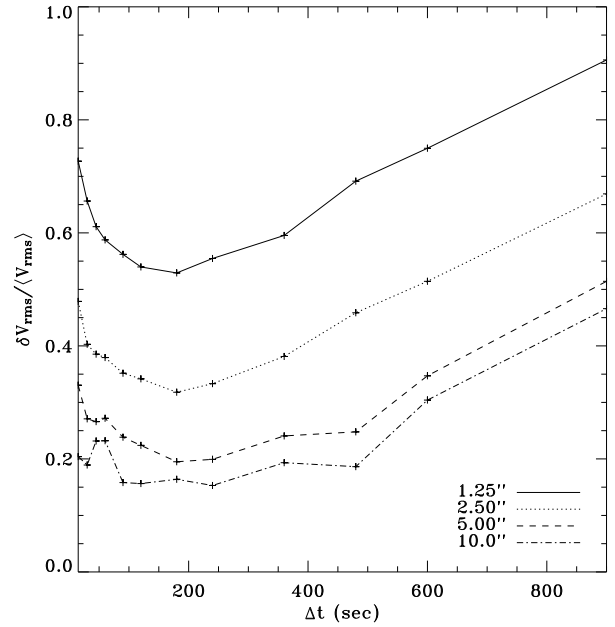


Fig. 10. Error on the x-component of the velocity as a function of the threshold on the granule lifetime. The different lines are for different resolutions of the multi-resolution decomposition; the solid line shows the raw case (no wavelet filtering). The optimal threshold clearly appears around 3 min.

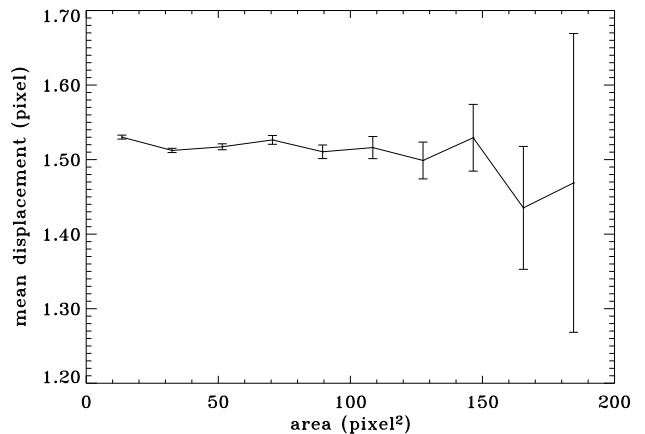


Fig. 11. Average distance between the granule centre of gravity for a pair of images as a function of the granule size.

grid whose elements have size δ . The velocity at a grid coordinate (x, y) is assumed to be the average of the velocity of granules whose average coordinates belong to the domain D around (x, y) (i.e. in $[x-\delta/2, x+\delta/2], [y-\delta/2, y+\delta/2]$). The spatial resolution of the velocity field is given by the mesh size δ . The x-component of the average velocity in D is given by

$$V_{x_p} = \frac{1}{N} \sum_{k \in D} V_{x_k} = \frac{1}{N} \sum_{k \in D} \frac{x_{k,n_f(k)} - x_{k,n_i(k)}}{\Delta t_k}$$

where N is the number of trajectories falling in D . The uncertainty on the value of V_{x_p} is then

$$\sigma_{V_{x_p}}^2 = \frac{1}{N^2} \sum_{k \in D} \frac{\sigma_{k,n_i}^2 + \sigma_{k,n_f}^2}{\Delta t_k^2}.$$

If we assume that the dispersion on the centre of gravity remains the same for the whole time series (σ_x) and that the time interval Δt_k is the same for all granules (i.e. all granules have the same lifetime Δt), then the expression of the dispersion of the average velocity in x is

$$\sigma_{V_{x_p}}^2 = \frac{1}{N^2} \sum_{i \in D} \frac{2\sigma_x^2}{\Delta t^2} = \frac{2\sigma_x^2}{N\Delta t^2}.$$

In this case, the error on the velocity varies like

$$\delta V = \frac{\sqrt{2}\sigma_x}{\sqrt{N}\Delta t}. \quad (1)$$

We see that precise velocity values need many granules in a grid element and a long time interval. In other words, errors are less if a coarse resolution in space and time is used. A trade off must be found (see below), but it is clear that this technique will be more appropriate to slowly evolving large-scale flows than to rapidly varying small-scale ones.

5.2. Influence of the granule lifetime

However, all granules do not have the same lifetime (see for example Hirzberger et al. 1999 or Paper I). In this case, it may be more appropriate to select only a subsample of the granules. For example, in the simple case where half of the N granules have a lifetime Δa_t and the other half a lifetime $\Delta b_t = 2\Delta a_t$, the error on the velocity is

$$\begin{aligned} \sigma_{a+b}^2 &= \frac{1}{N^2} \left(\sum_{i \in D, \Delta t_i = \Delta a_t} \frac{2\sigma_x^2}{\Delta a_t^2} + \sum_{i \in D, \Delta t_i = \Delta b_t} \frac{2\sigma_x^2}{\Delta b_t^2} \right) \\ &= \frac{1}{N^2} \left(\frac{N\sigma_x^2}{\Delta a_t^2} + \frac{N\sigma_x^2}{4\Delta a_t^2} \right) = \frac{5\sigma_x^2}{4N\Delta a_t^2}. \end{aligned}$$

If we take only the $\frac{N}{2}$ granules with the largest lifetime Δb_t into account, we obtain

$$\begin{aligned} \sigma_b^2 &= \frac{2^2}{N^2} \sum_{i \in D, \Delta t_i = \Delta b_t} \frac{2\sigma_x^2}{\Delta b_t^2} = \frac{4}{N^2} \frac{N\sigma_x^2}{4\Delta a_t^2} \\ &= \frac{\sigma_x^2}{N\Delta a_t^2} \leq \sigma_{a+b}^2. \end{aligned}$$

Therefore, the errors are smaller when considering only the granules with the longest lifetime.

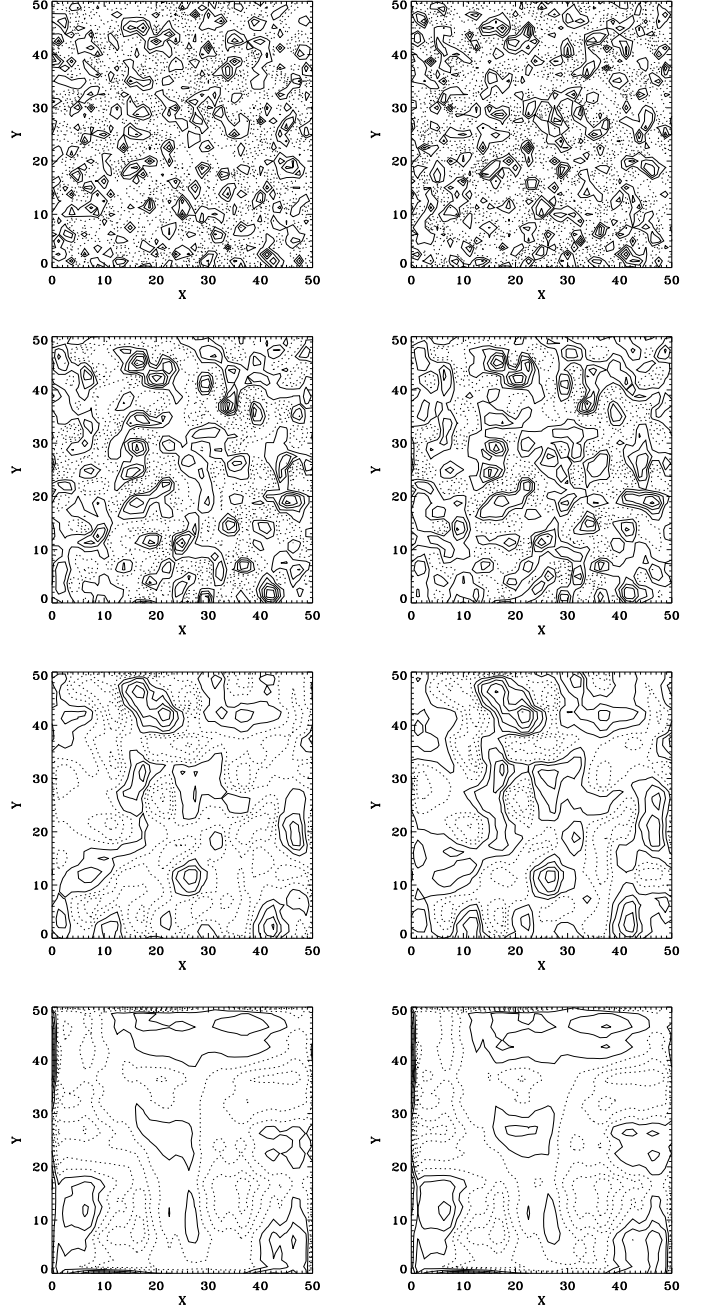


Fig. 12. Two views of the divergence field at different resolution. The difference between the left and right flow fields is the noise introduced by the Earth’s atmosphere. In the first row no filtering has been applied and common features are barely identifiable. The following rows show filtered data according to multi-resolution representation (see Paper I) with a resolution divided by 2 from one row to the next. The mesh size is 10 pixels (1’/25) and the flow is an average over ~ 1.5 hr. X and Y are in arcsec.

This result shows that some selection of “valid granules” may improve the quality of the velocity field. We thus impose a lower threshold on the granule lifetime to eliminate short-lived structures. This threshold has to be

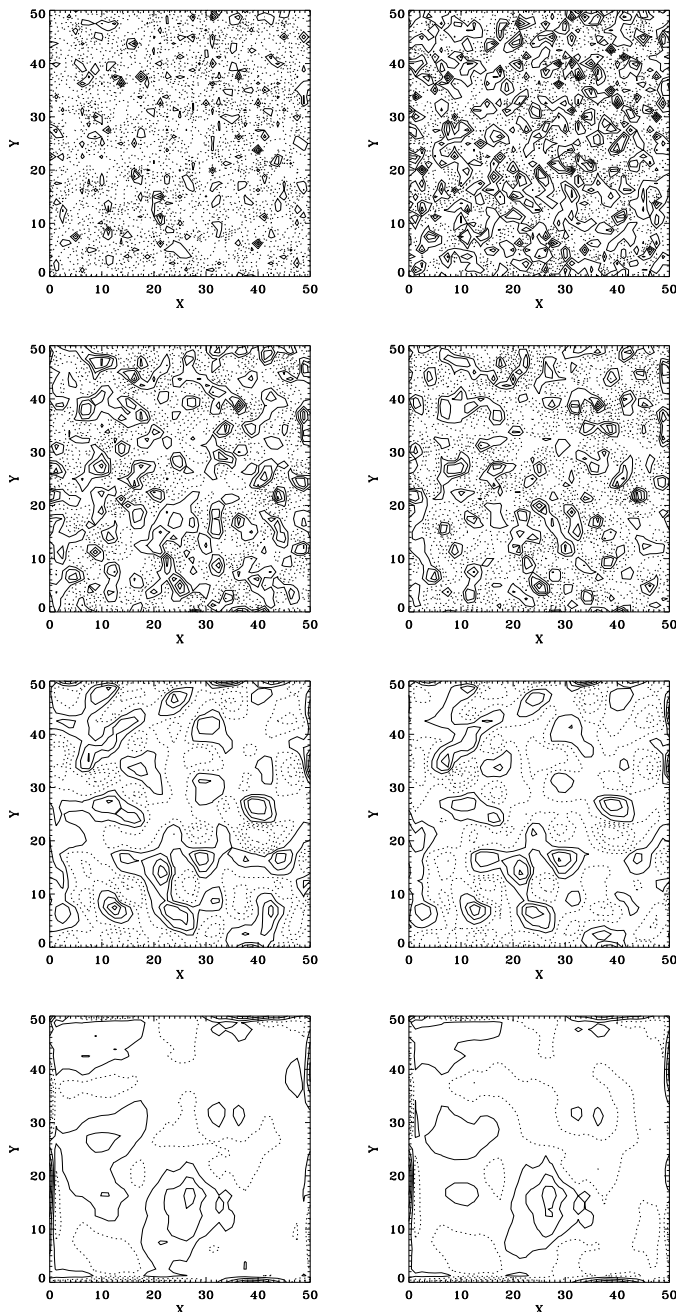


Fig. 13. Same as in Fig. 12 but for the z-component of the curl field.

determined empirically and depends on the filling factor of the grid. (We need to avoid grid points with no data, see Paper I.) This strategy may be improved by computing the average velocity for various thresholds, starting with the highest one. Since granules with long lifetimes are rare the number N is small and the error is large. By reducing the threshold, the number of granules increases rapidly and the error decreases. For some optimal threshold, the error ceases to decrease as the increase in granule number no longer compensates for the diminishing value of Δt (see Eq. 1). This process is illustrated in Fig. 10 where we show the dispersion of velocity differences between the

two independent data sets as a function of the threshold on the granule lifetime. Clearly, for these data the optimal threshold is around 3 min.

5.3. Influence of the granule size

It is also interesting to study the influence of the granule size on the error for the granule centre of gravity. We would expect a smaller error in the case of large granules, as these are defined by a larger number of pixels. A selection on the granule size could then also improve the precision on the velocity field. Figure 11 shows an estimation of the error on the granule position for various granule size intervals. The precision increases only slightly with the granule size, and the improvement is at most 0.05 pixels. This means that the error on the velocity will not change much either. This small improvement in the error is too weak to compensate for the increase in the error on the velocity due to the decrease in the number of granules as their size increases.

6. Error propagation to the final maps

Following the algorithm described in Paper I (but see also Sect. 5.1), we now compute the velocity fields of the two independent time series at a different resolution (see Paper I). A comparison between the two fields shows the influence of the distortion induced by the Earth’s atmosphere and the efficiency of MRA in revealing the flow patterns on the different scales. The results are illustrated by Figs. 12 and 13, which show the horizontal divergences and the vertical component of vorticity, respectively. This flow field is the average velocity over a time lapse of $\Delta t = 87$ min including the preceding sequence and with no distinction between the “bad” and “good” sequences. Actually, we first computed the velocity fields using the “good” sequence and then extended the computation to the whole set. We observed that the dispersion between the two independent sequences was still reduced when using the whole set of data showing that, for the determination of the large-scale mean flow, the observed degradation in the distortion is not influential.

In Table 3, we quantitatively summarise the dispersion of the results as a function of the resolution for unfiltered images. This table has been obtained with the whole time series (87 min), using a velocity pixel of $1.25''$ and removing all granules with a lifetime less than 180 s. We computed the rms velocities, divergences and curls, of the maps issued from the multi-resolution decomposition. The “uncertainties” shown along the numbers give the amplitude of the fluctuations generated by the Earth’s atmospheric distortion. This table shows the decreasing influence of distortion with increasing scale. It also shows that, as expected, velocity gradients (divergence and the z-component of the vorticity) suffer much more from the noise and that the curl is certainly the quantity most sensitive to image quality. The values of the correlations between the results issued from the two independent series

Resolution (pixel size)	V_{rms}	C_v	$(\text{Div } V)_{\text{rms}}$	C_d	$(\text{Curl } V)_{\text{rms}}$	C_c	Turbulence	
1.25''	920 km	700±695	0.49	7.1±7.0	0.45	5.7±7.0	0.22	880±224
2.50''	1840	478±342	0.74	3.8±2.8	0.69	2.9±3.0	0.45	893±122
5.00''	3680	340±172	0.87	1.6±0.9	0.89	1.2±0.9	0.73	890±94
10.0''	7360	205±92	0.90	0.58±0.24	0.94	0.41±0.24	0.85	896±65

Table 3. Rms velocities, divergences and curls, of the maps issued from the multi-resolution analysis of the whole time series. The first row is raw data (no wavelet filtering) while the next rows shows the numbers issued from the wavelet-filtered maps. Velocities and turbulence are in m/s, divergence and curl in 10^{-4}s^{-1} .

Resolution (pixel size)	V_{rms}	C_v	$(\text{Div } V)_{\text{rms}}$	C_d	$(\text{Curl } V)_{\text{rms}}$	C_c	Turbulence	
1.25''	920 km	597±330	0.85	6.8±4.2	0.81	5.0±4.2	0.66	680±193
2.50''	1840	466±162	0.94	4.0±1.7	0.91	2.7±1.7	0.81	692±105
5.00''	3680	350±80	0.97	1.8±0.4	0.97	1.2±0.4	0.95	689±78
10.0''	7360	209±40	0.98	0.63±0.1	0.98	0.42±0.1	0.96	694±53

Table 4. Same as Table 3 but for $k - \omega$ filtered data. Note the reduction in the dispersion of the results.

Resolution (pixel size)	V_{rms}	C_v	$(\text{Div } V)_{\text{rms}}$	C_d	$(\text{Curl } V)_{\text{rms}}$	C_c	Turbulence	
0''875	644 km	722±534	0.73	11±9.7	0.64	10±9.7	0.54	528±288
1''75	1288	528±258	0.88	6.3±3.7	0.83	4.5±3.8	0.65	532±143
3''50	2576	403±128	0.95	2.7±0.9	0.94	1.8±0.9	0.87	533±75
7''	5152	284±65	0.97	1.2±0.3	0.97	0.7±0.3	0.94	533±45

Table 5. Same as Table 4 but for a smaller velocity pixel.

(C_v , C_d and C_c) quantitatively indicate the similarity of the fields. Here too, filtered fields are much better correlated, up to 90% on the velocity field. As shown below, this correlation is still improved when using $k - \omega$ filtered data.

In this table, we also give a ‘turbulent velocity’, which is the mean rms dispersion of granule velocities. Indeed, in each velocity pixel we take the mean velocity of the granules falling in this very pixel; however, while computing this mean velocity, we also have access to the dispersion around this mean. This mean (over the whole field of view) dispersion represents the random motion of granules around their drift by large-scale flows. This table shows that, although this quantity suffers (also) from image quality, it is almost independent of scale. This independence is expected since this quantity measures the proper motion of granules and therefore their intrinsic kinetic energy, which should not vary from place to place.

Table 4 gives the same quantities but for the $k - \omega$ filtered sequence. We note the strong reduction of the noise, almost a factor 2, on all scales and the strong improvement of correlation between the results of the two independent series. Moreover, the dispersion of the velocities is reduced in the same proportion as displacement of granules (i.e. $\frac{330\text{m/s}}{695\text{m/s}} \sim \frac{0.4\text{pix.}}{0.7\text{pix.}}$). The comparison of the values of turbulence in Tab. 3 and 4 shows the influence of the Earth’s atmospheric noise on the random motion of granules.

Table 5 gives another view of this velocity field using a smaller mesh size. Here we computed the velocity amplitudes that are traced by granules when they can be considered as passive scalars, i.e. on a scale larger than 2500 km. Numbers show that on that scale the velocity field has an amplitude of 400 m/s and that such a measurement is still uncertain by 30%. This is about the same for the divergence, but it rises to 50% for the vorticity. The more intense fluctuations compared to Table 4 come from the smaller scales involved. The weaker ‘‘Turbulence’’ values come from the empty bins which are more numerous.

These results show that, when independent images series are available, the use of the CST algorithm authorizes a tight control on the role of the noise induced by the Earth’s atmospheric distortion.

7. Conclusions

In this paper we have tried to show the various influences of the noise generated by the Earth’s atmosphere when one measures the horizontal velocity field at the surface of the sun through granule tracking.

For this purpose we compared two time series of images of the solar surface separated by at most a few seconds; they thus represent the same solar signal but with a different noise (essentially, distortion from the Earth’s atmosphere). We measured the position of the granules in the two time series and used these data to determine the amplitude of the noise. We could thus test the pre-processing

that could first be applied to the images, namely a $k-\omega$ filtering and the destretching. The comparison between the pre-processed series and the raw one allowed us to evaluate the efficiency of the pre-processing. It turns out that $k-\omega$ filtering significantly reduces the noise while destretching, even if reducing the fluctuations, not only cannot reduce it, but amplifies it when distortion increases.

We also found that the CST algorithm that tracks coherent structures (essentially granules) could easily go across sequences of images with decreased image quality. This is because all granules are not affected evenly by distortion and granules whose trajectories are too perturbed by atmospheric noise are eliminated; they thus do not input noise in the final velocity field. This is clearly a feature that algorithms based on local correlations of images cannot authorize.

We also studied how the distortion noise affecting granules positions introduces some noise into the interpolated velocity fields. We thus showed that the lifetime of granules was an important parameter and that short-lived granules should be eliminated. The trade-off between granule number (the more numerous the granules, the better sampled the velocity field) and noise intensity seems to be, for our sequence, around 3 min. It is clear that, if the atmospheric noise is more intense, this threshold should be increased. With the decomposition of the velocity on the Daubechies wavelets (see Paper I), we could evaluate the impact of the noise on different scales and show that errors on velocities decrease with increasing scale, as expected. More precisely, we could show that on a scale of 2500 km, i.e. on the scale where granule motions trace the large-scale flows (Rieutord et al., 2001), the typical velocities, around 400 m/s, are still noised at a 30% level. Nevertheless, one can recognize, on the wavelet-filtered maps, common patterns between the two time series, all the more easily when the scale is large.

The next steps are now obvious: with new cameras with fast reading sensors (like CMOS), it is easy to increase the time sampling by a factor 10. In this case the $k-\omega$ filtering will be much more efficient at reducing the noise on the granule motion. Hence, with an increased time-sampling we expect to reduce the noise in two ways: first, by an improved efficiency of the $k-\omega$ filter and second by a factor \sqrt{N} from the N images sharing the same solar signal.

The tools developed here seem to perform quite efficiently on the numerical side and therefore allow for the treatment of much larger fields of view.

Finally, we did not discuss the results in terms of solar turbulence. Let us mention that numbers, like the amplitude of velocity on a 2.5 Mm scale, agree with previous determinations (e.g. Brandt et al., 1991). However, it is clear that (solar) fluid mechanics should be discussed, such as the scale dependence of flow features. This is beyond the scope of this paper but will be the subject of forthcoming work.

Acknowledgements. RT wishes to thank the French ministry of education for its financial support through the CALAS project. We are most grateful to Peter Brandt who kindly allowed us to use the extraordinary eleven-hour sequence obtained at the SVST of La Palma.

References

- Brandt, P., Ferguson, S., Scharmer, G., et al. 1991, *Astron. & Astrophys.*, 241, 219
- Dorotovič, I., Sobotka, M., Brandt, P. N., & Simon, G. W. 2002, *A&A*, 387, 665
- Getling, A. V. & Brandt, P. N. 2002, *A&A*, 382, L5
- Hirzberger, J., Bonet, J. A., Vázquez, M., & Hanslmeier, A. 1999, *ApJ*, 515, 441
- November, L. J. & Simon, G. W. 1988, *Astrophys. J.*, 333, 427
- Potts, H. E., Barrett, R. K., & Diver, D. A. 2003, *Sol. Phys.*, 217, 69
- Rieutord, M., Roudier, T., Ludwig, H.-G., Nordlund, Å., & Stein, R. 2001, *Astron. & Astrophys.*, 377, L14
- Rieutord, M., Roudier, T., Roques, S., & Ducottet, C. 2007, to appear in *A & A*, 1
- Roudier, T., Lignières, F., Rieutord, M., Brandt, P. N., & Malherbe, J. M. 2003, *A&A*, 409, 299
- Simon, G. W., Brandt, P. N., November, L., Scharmer, G. B., & Shine, R. A. 1994, in *Solar Surface Magnetism*, ed. R. Rutten & C. Schrijver (Kluwer), 261
- Simon, G. W., Brandt, P. N., November, L., Shine, R., & Strous, L. 1995, in *Proc. of 4th SOHO Workshop: Helioseismology (ESA SP-376)*, 223
- Sobotka, M., Brandt, P. N., & Simon, G. W. 1997a, *A&A*, 328, 682
- Sobotka, M., Brandt, P. N., & Simon, G. W. 1997b, *A&A*, 328, 689
- Sobotka, M., Brandt, P. N., & Simon, G. W. 1999a, *A&A*, 348, 621
- Sobotka, M., Vázquez, M., Bonet, J. A., Hanslmeier, A., & Hirzberger, J. 1999b, *ApJ*, 511, 436
- Title, A. M., Tarbell, T. D., & Topka, K. P. 1987, *ApJ*, 317, 892